Origins and consequences of asymmetric nano-FTIR interferograms

GERGELY NÉMETH,[1,2,*] HANS A. BECHTEL,[3,$] AND FERENC BORONDICS,[1,#]

[1]SOLEIL Synchrotron, L'Orme des Merisiers, RD128, Saint Aubin, France 91190
[2]Wigner Research Centre for Physics, 29-33 Konkoly-Thege str. Budapest, Hungary, 1121
[3]Advanced Light Source, Lawrence Berkeley National Laboratory, 1 Cyclotron Road, Berkeley, CA USA 94720
[*]gergely.nemeth@synchrotron-soleil.fr, [$]habechtel@lbl.gov, [#]ferenc.borondics@synchrotron-soleil.fr

Abstract:

Infrared scattering-type near-field optical microscopy, IR s-SNOM, and its broadband variant, nano-FTIR, are pioneering, flagship techniques for their ability to provide molecular identification and material optical property information at a spatial resolution well below the far-field diffraction limit, typically less than 25 nm. While s-SNOM and nano-FTIR instrumentation and data analysis have been discussed previously, there is a lack of information regarding experimental parameters for the practitioner, especially in the context of previously developed frameworks. Like conventional FTIR spectroscopy, the critical component of a nano-FTIR instrument is an interferometer. However, unlike FTIR spectroscopy, the resulting interference patterns or interferograms are typically asymmetric. Here, we unambiguously describe the origins of asymmetric interferograms recorded with nano-FTIR instruments, give a detailed analysis of potential artifacts, and recommend optimal instrument settings as well as data analysis parameters.

1. Introduction

Infrared spectroscopy has been dominated by Fourier-transform (FT) instruments shortly after the first commercial FTIR spectrometer appeared on the market in the 1960s. [1] Seminal works of Fellgett [2] and Jacquinot [3] established the advantages of spectroscopic interferometry over grating instruments and led to a general layout where the radiation probing the sample is conditioned by first passing through an interferometer; in modern instruments, most frequently using a configuration introduced by Michelson and Morely, *a.k.a. the Michelson interferometer*. [4] Today, such Fourier-transform infrared instruments are ubiquitous in both industrial and scientific settings and contribute to a plethora of research. They provide easy access to rotational, vibrational and electronic absorption spectra. However, to determine complex value functions, e.g., the complex refractive index ($\tilde{n}$), one needs to apply the Kramers-Kronig transformation, [5, 6] which require low- and high-energy extrapolations as the integrals are formulated from zero to infinity.

In the 1960s, an alternative method, called Dispersive Fourier Transform Spectroscopy (DFTS), was developed to more directly determine complex optical functions, achieved by placing the sample inside the interferometer (Fig. 1). [7, 8] This asymmetric Michelson interferometric approach was further developed through the late 1980s [9–11], but it was never commercialized due to technical limitations at the time, [12] as well as a relatively limited commercial gain over existing solutions.

Both FTIR and DFTS instruments measure a real-value dataset: the detector intensity as a function of the optical path difference (OPD) of the two interferometer mirrors. The resulting interferogram is subsequently Fourier-transformed to yield a complex-value dataset. In FTIR the phase is not related to the sample and reflects the interferometer's characteristics (inaccuracies of optical elements, misalignment, beamsplitter dispersion) and sampling inaccuracies. Most often, the phase interferogram is used to maximize the amplitude algorithmically. [1] In contrast, the

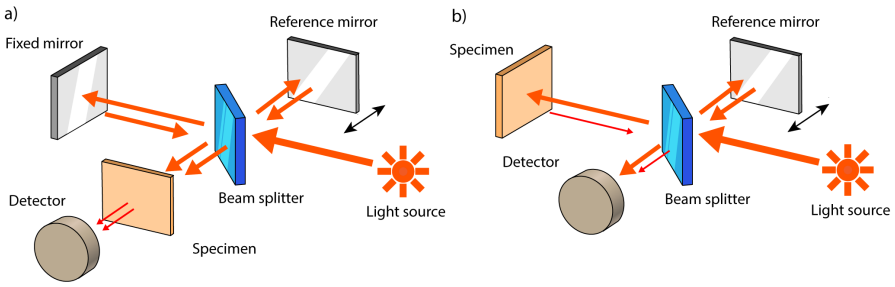

Fig. 1. Schematics of the arrangement (a) conventional FTIR and (b) DFTS setups. In the case of simple FTIR the sample is located after the interferometer, while in the case of DFTS the sample is inserted in the arm with the fixed mirror. Reflective samples can replace the fixed mirror completely (like in b), while in transmission mode the sample is inserted between the fixed mirror and the beamsplitter.

phase spectrum in DFTS, where the light passes through the sample inside the interferometer and thus suffers a particular phase shift, carries information about the sample. By using the amplitude and phase information, DFTS instruments can directly measure the complex dielectric response of a material.

Although DFTS was never commercialized, another IR microscopy technique, scattering-type Scanning Near-field Optical Microscopy (s-SNOM), uses the same asymmetric Michelson arrangement and has achieved commercial success. This technique enables infrared spectroscopic measurements at the nanoscale, with a spatial resolution of several orders of magnitude better than diffraction-limited, far-field infrared techniques.

1.1. Scattering SNOM and nano-FTIR

A typical s-SNOM setup consists of an infrared source and an atomic force microscope (AFM) located within an asymmetric Michelson interferometer. In this case, the fixed mirror is replaced by the ensemble of a focusing mirror, the AFM tip, and the sample, as depicted in Fig. 2. Light enters the interferometer and the beamsplitter directs half the light to the moving reference mirror while the other half is focused onto the apex of the AFM tip. When the sample is brought into close proximity of the tip, the optical fields locally interact in the near field and cause scattering that can be detected in the far field. The scattered light is collected by the same focusing mirror and recombined with the light from the reference mirror before being measured by an infrared detector. The interaction volume is defined by the AFM tip sharpness, and is usually on the order of tens of nanometers, allowing spatial resolution well beyond the far-field diffraction limit.

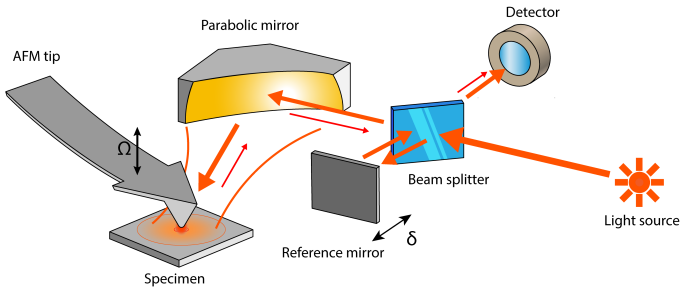

Fig. 2. Schematic representation of a s-SNOM setup.

To separate the weak near-field scattering from the intense background scattering, s-SNOM measurements combine higher harmonic demodulation and interferometric signal amplification. The AFM operates in tapping mode to modulate the scattering amplitude and the detector signal is demodulated at harmonics of the tip oscillation frequency (nΩ). Because the near-field interaction is non-linear with sample distance, higher harmonic detection leads to suppression of the far-field scattered light, which is nominally linear with sample distance. Additionally, mixing the back-scattered light (E_N) with the beam from the reference mirror of the interferometer (E_R) results in signal level enhancement by $E_N E_R$ and phase modulation in the interference term. With monochromatic illumination, the reference mirror movement is typically modulated at a fixed frequency in a pseudo-heterodyne detection scheme that further suppresses background and extracts the amplitude and phase of the near-field scattering [13]. For broad-band illumination, the reference mirror is moved linearly over a fixed distance and the demodulated signal is recorded as a function of mirror position to collect an interferogram. The subsequent nano-FTIR interferogram is then Fourier-transformed to yield the amplitude and the phase of the scattered light. [14]

Here, we will discuss the analogies between DFTS and s-SNOM and unambiguously explain the origin and practical consequences of the recorded asymmetric interferogram.

2. Origin of the asymmetry

In a Michelson interferometer, the beamsplitter divides the incoming beam in two (we consider an ideal 50:50 beamplitter). Considering broadband illumination, the incoming collimated beam contains a broad range of wavelength components. The interferogram is the sum of the interference patterns of the individual wavelength components. First, let us consider a single wavelength component. Its electric field is described as

$$\mathbf{E}(\mathbf{r},t) = \mathbf{E}_0 \exp\left[i(\Phi_r(k) + \mathbf{k}\cdot\mathbf{r} - \omega t)\right]. \tag{1}$$

The part of the beam that is directed to the reference arm of the interferometer is reflected back by a moving mirror and written as

$$\mathbf{E}_R(\mathbf{r},t) = \frac{1}{2}\mathbf{E}_0 \exp\left[i(\Phi_r(k) + \mathbf{k}\cdot\mathbf{r} - \omega t + k\cdot\delta)\right], \tag{2}$$

where $\delta/2$ is the displacement of the moving mirror from the zero path difference position of the two arms and $\Phi_r(k)$ is a random initial phase for each wavelength component.

In the asymmetric setup, the sample is located in the stationary interferometer arm. The interaction of the light with the sample is described by the complex insertion loss in DFTS and formulated as $L(k)\exp[\Phi_L(k)]$. The exact expression of the insertion loss depends on the interaction that influences the backward propagation of the electromagnetic field in this arm. For s-SNOM, the dominant effect is the back-scattering, originating from the tip-sample interaction. The scattered field from the sample arm is

$$\mathbf{E}_S(\mathbf{r},t) = \frac{1}{2}\mathbf{E}_0 L(k) \exp\left[i(\Phi_r(k) + \mathbf{k}\cdot\mathbf{r} - \omega t + \Phi_L(k))\right]. \tag{3}$$

Note, that the initial $\Phi_r(k)$ random phase remains the same in both arms because the Michelson interferometer with an ideal beamsplitter realizes only amplitude division. Finally, the split beams recombine, and the electric field at the detector can be written as

$$\mathbf{E}_D(r,t) = g(k,x)\exp\left[i(\mathbf{k}\cdot\mathbf{r} - \omega t)\right], \tag{4}$$

where

$$\mathbf{g}(k,x) = \frac{1}{2}\mathbf{E}_0(k)\left(L(k)\exp\left[i\Phi_L(k)\right] + \exp\left[ik\delta\right]\right). \tag{5}$$

The detector intensity is proportional to $\mathbf{E}_D\mathbf{E}_D^*$, which leads to

$$I_D(k,\delta) = \frac{1}{4}[1 + L^2(k)]\mathbf{E}_0(k)\mathbf{E}_0^*(k) + \frac{1}{2}L(k)\cos[\Phi_L(k) - k\delta]\mathbf{E}_0(k)\mathbf{E}_0^*(k). \tag{6}$$

Here, the second term describes the interference and it is recorded as the mirror is moving (changing δ). The amplitude of the recorded cosine interferogram is set by the amplitude $L(k)$ of the loss function, while its phase is controlled by the phase shift $\Phi_L(k)$.

For incoherent, broadband illumination, the full interferogram is the incoherent sum of all the individual cosine interferograms of each wavelength component.

$$I_D(\delta) = \int_{-\infty}^{\infty} I_D(k,\delta)\,dk = \tag{7}$$

$$\int_{-\infty}^{\infty} \frac{1}{4}[1 + L^2(k)]I_0(k)\,dk + \int_{-\infty}^{\infty} \frac{1}{2}L(k)I_0(k)\cos[\Phi_L(k) - k\delta]\,dk, \tag{8}$$

where $I_0(k) = \mathbf{E}_0(k)\mathbf{E}_0^*(k)$ is the intensity of the incoming radiation. The first term of Eq. 8 is independent of the reference mirror position δ and thus gives only a constant offset to the interferogram. The varying part of the interferogram which contains information is the second term. From Eq. 8, we see that $L(k)$ changes the amplitude while $\Phi_L(k)$ shifts each component compared to the ZPD position. This results in a significant change in the shape of the full interferogram. In the end, we see that the complex insertion loss $\hat{L}(k) = L(k)\cdot\exp i\Phi_L(k)$ drives the asymmetry. The exact formula for the insertion loss is defined by the physical interaction between the sample and the incoming light. We showcase the effect of insertion loss on the interferogram in Fig. 3.

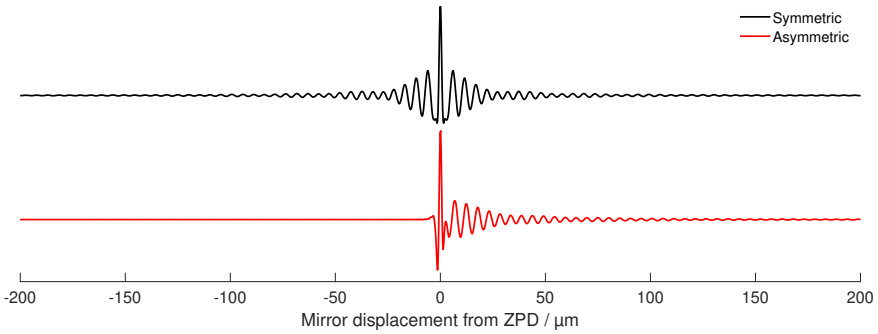

Fig. 3. Comparison of symmetric (conventional FTIR) and asymmetric (DFTS) interferograms. It considers a reflective half-infinite SiC mirror placed after the interferometer (symmetric) or in the interferometer, replacing the fixed mirror (asymmetric)

In the following, we consider a DFTS arrangement with a SiC sample in the position of the fixed mirror. The loss function in this case is defined as the Fresnel reflection coefficient. For the sake of simplicity, we assume normal incidence, thus the insertion loss becomes $\hat{L}(k) = r(k) = (n_{SiC}(k) - 1)/(n_{SiC}(k) + 1)$. Using (8) and ignoring the DC part of the signal, we get the highly asymmetric interferogram shown as the red curve of Fig. 3.

From Fig. 3, we see that the asymmetry modifies the positive pathlength difference part of the interferogram. The reason for this is that physical processes like scattering, reflection, and emission always induce a positive phase shift due to causality.

In DFTS interferograms the asymmetry contains information about the sample's complex optical properties, while in conventional FTIR, the phase spectrum (phase of the Fourier transform of the interferogram) does not tell anything about the sample.

The insertion loss of a sample can be retrieved through a reference measurement as follows:

$$\hat{L}(k) = \int_{-\infty}^{\infty} I_S(\delta) \exp(2\pi i k \delta)\, d\delta \Big/ \int_{-\infty}^{\infty} I_R(\delta) \exp(2\pi i k \delta)\, d\delta \tag{9}$$

$$= FT(I_S(\delta))/FT(I_R(\delta)), \tag{10}$$

where the subscripts S and R stand for sample and reference, respectively.

Furthermore, if the complex insertion loss is linearly related to the optical functions of the sample, DFTS provides a direct measurement.

2.1. Nano-FTIR interferograms

We can explain the nano-FTIR interferogram in the framework of DFTS presented above. The key is to find the insertion loss that describes the scattering of the tip-sample ensemble. The calculation of the amplitude and phase of the back-scattered light can be done in different ways as numerous theoretical methods have been used to approximate the solution of the scattering problem. [15–23] A widely used and easily implementable tip-sample interaction model, the so-called finite dipole model (FDM) treats the problem with a quasi-electrostatic approach and describes the main characteristics of the scattering almost quantitatively. [21]

The main quantity that we are looking for is the complex scattering coefficient $\sigma(k)$ which relates the incoming and the back-scattered fields by $E_s = \sigma(k)E_{inc}$. The FDM model provides a closed-form solution for the scattering coefficient. [21] σ inherits its wavelength dependence from the dielectric function of the sample. As σ characterizes the backward propagating optical field, it can be used as the insertion loss we were looking for.

In a real measurement, however, the acquired signal is not directly proportional to the scattering coefficient. The detected signal contains a significant background component hindering the tip-scattered light originating from the near-field interaction. To retrieve the pure near-field signal, the AFM works in tapping mode vibrating the tip at frequency Ω. Then, the acquired time-dependent signal is then demodulated at higher harmonics $n\Omega$. To gather a similar quantity from the FDM model, we implement the modulation for the scattering coefficient σ. Then, similarly to the real measurement by demodulating the time-dependent signal at the nth harmonic of Ω, we get σ_n.

By using the FDM model to derive $\sigma_n(k)$ and substituting it for the insertion loss we can calculate the nano-FTIR interferograms and assess their asymmetry. To showcase the effect of different material responses we created a dielectric function to model theoretical material possessing three typical excitation types in the mid-infrared spectral range. We used this to calculate the amplitude and phase of the 2nd harmonic scattering coefficient. This dielectric function and the scattering spectrum can be viewed in Fig. S1. At around zero frequency, we added a typical Drude excitation, at 800 cm^{-1} a surface polariton excitation, and at 1423 cm^{-1} we imitate a simple vibrational excitation where the real part of the dielectric function remains positive.

For a Lorentzian oscillator with only positive real values, the scattering phase follows the shape of the imaginary part of the dielectric function. This is usually the case of weak molecular vibrations. The phase of the scattering signal is sensitive and grows large when the real part of the dielectric function falls below zero, which is typical for collective excitations like surface polaritons. This sensitivity makes s-SNOM ideal to study surface excitations, which is shown by the numerous publications from studies on plasmons in graphene and carbon nanotubes to phonons in polar dielectrics [24–31].

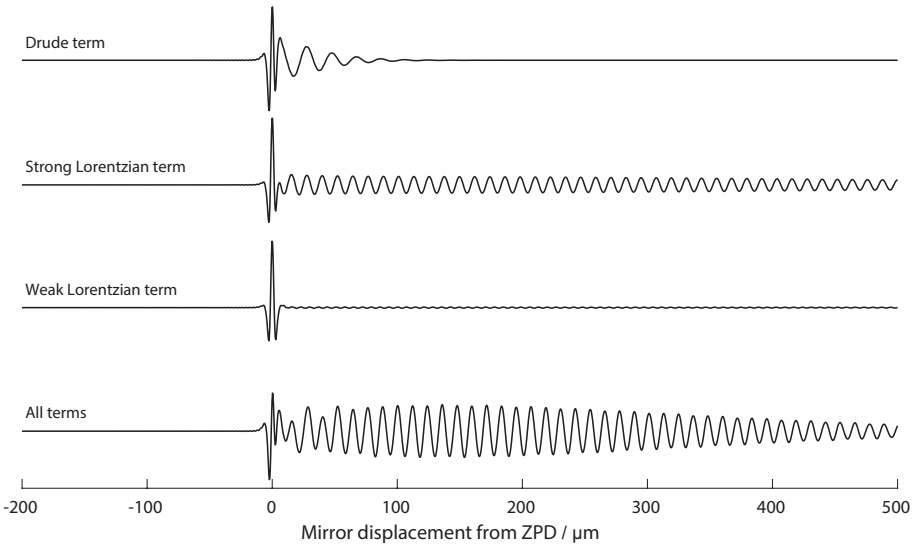

Fig. 4. Model interferograms based on Eq. 8, composed of different terms from the model dielectric function to determine the scattering coefficient using FDM model.

Based on Eq. 8, the stronger and broader the scattering phase spectrum, the more asymmetry will appear in the interferogram. To provide insight into this statement, in Fig. 4 we present the calculated interferograms for theoretical materials exhibiting only one of the above-mentioned excitations at a time. Fig. 4 shows how the broad Drude peak introduces pronounced asymmetry with a fast decay of the interferogram while the similarly strong, but narrower Lorentzian peak introduces a much longer-lasting interferogram for the positive path lengths. With the weak oscillator, the asymmetry is not that clear as the phase shift is small and concentrated only to a few wavelengths.

3. Model validation

To validate our description of the interferograms, we modeled and measured the nano-FTIR interferogram of 300 nm SiO_2 layer on top of silicon. The broadband s-SNOM measurements were done at the SMIS beamline of the SOLEIL synchrotron, the French national synchrotron facility, with a commercial s-SNOM manufactured by Attocube system AG (Haar, Germany). The incident synchrotron radiation was split by a ZnSe beamsplitter and the transmitted beam was focused on the apex of a platinum-coated AFM tip by an off-axis parabolic mirror. The reflected part of the beam entered the reference arm with the moving mirror actuated by a piezo stage capable of moving 800 μm. We recorded the full interferogram of the thermally grown SiO_2 layer using the full range of the piezo actuator acquiring 2048 points which resulted in 0.39 μm spatial sampling. The integration time for each pixel was 13 ms and the tapping amplitude of the tip was set to 100 nm. Data was recorded for higher-harmonics up to the 4th order but in the following, we use 2nd harmonic near-field signals in our analysis.

For modeling, we used FDM as described above to calculate the second harmonic demodulated amplitude and phase spectrum to derive the interferograms. The dielectric function for the SiO_2 layer was obtained from the literature model reported by Kischkat et al. [32]. Fig. S2 renders the dielectric function and the second harmonic amplitude and phase spectra that was used in the interferogram calculation. The DFTS insertion loss is defined as $L_n(k) = \sigma_n(k) = s_n(k) \exp[i\varphi_n(k)]$, where $s_n(k) = s_{n,SiO_2}/s_{n,Au}$ and $\varphi_n(k) = \varphi_{n,SiO_2} - \varphi_{n,Au}$, because all the data in the measurements were normalized to a reference measurement on gold. In all of our

studies, both calculated and measured amplitude and phase values were normalized to that of gold substrates. We expect a definite asymmetry with moderate decay caused by the broad, intense phase peak ranging from around 1100 cm^{-1} to 1500 cm^{-1} originating from the phonon band of the SiO_2.

Our calculations describe the corresponding measurements nearly perfectly. Fig. 5 shows the comparison of the model result (black) and the measured interferogram (red). The interferogram was calculated by Eq. 8 using the second harmonic scattering coefficient as the insertion loss described above. The small difference between the two curves can originate from the inaccuracy of the dielectric function of the SiO_2 layer and the limitations of the simple FDM model. Still, with these limitations, the DFTS-based interferogram calculation described above can reproduce and explain the asymmetry of nano-FTIR interferograms extremely well.

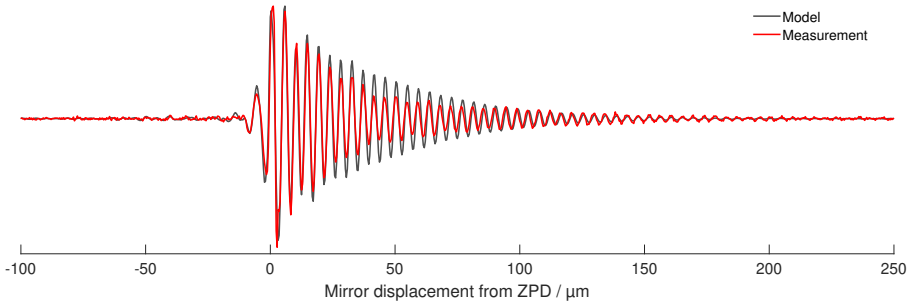

Fig. 5. Measured (red) and calculated (black) interferogram of the 300 nm SiO_2/Si sample.

As we showed in this section, our model can replicate and explain nano-FTIR interferograms, thus it can be confidently used to explore the effect of various measurement artifacts and data-processing schemes on the final spectrum. In the following, we discuss the most important considerations one has to make during measurements and the processing of raw interferograms.

3.1. Effect of temporal coherence

In real nano-FTIR setups, the light source is usually a pulsed mid-IR laser. Commercially available instruments use lasers with a pulse width $\approx 100-200$ fs, and high, MHz, repetition rate. [33–35] The advantages of these sources are the large spectral irradiance and the spatially coherent beam which makes them ideal for focusing. However, the possibility of near-field nano-FTIR measurements using thermal (Globar) sources was also demonstrated. Their advantage is the broad spectral range, but, due to their low spectral radiance and spatial coherence, the resulting near-field signal is far lower quality. [14] Alternatively, nano-FTIR spectroscopy with high-temperature plasma light sources was also demonstrated which improves the spatial coherence of thermal sources, thus providing better focusing. [36] Furthermore, a third possibility is using synchrotron sources [37] as the spectral range of a common infrared beamline ranges from the THz up to the near-IR/visible range providing high spectral radiance and diffraction-limited focusing.

The important difference between light sources is temporal coherence. For temporally coherent sources, such as pulsed lasers, the asymmetry of the interferogram was explained by optical free induction decay (optical FID) previously. [38] Optical FID requires the fast switch-off of the excitation or the fast detuning of the resonance of the sample thus usually measured in the time domain. [39, 40] The time delays during the re-emission process for each wavelength result in phase-shifted but coherent fields and distort the time domain shape of the back-scattered pulse,

which represents the impulse response function of the sample. In the asymmetric Michelson-interferometer arrangement, the cross-correlation of the original and the back-scattered pulses is recorded as the interferogram.

However, thermal sources or typical synchrotron radiation don't provide temporally coherent pulses, i.e., the phase between the different wavelength components varies randomly ($\Phi_r(k)$ in Eq. 2 and 3).[1] The final interferogram, however, looks the same as with coherent excitation. This is because a Michelson interferometer realizes amplitude division thus the initial phase $\Phi_r(k)$ is the same in both arms and does not play a role in the interferogram formation. This means that formally both coherent and incoherent cases result in the same formula (Eq. 8) and the interferograms look the same.

We want to note that in both cases the origin of the asymmetric interferogram is the phase shift of each wavelength component by the scattering process. FID signal is a special case when using coherent radiation, but the resulting interferogram is the same with or without temporal coherence. In Fig. S4, we show this in detail for coherent and incoherent sources.

4. Implications for measurement and data processing

In FTIR, as shown by Eq. 10, the frequency response of the sample is calculated by Fourier transforming the interferogram. As extensively, and widely described, the preprocessing of the interferograms before Fourier transformation is a critical step to suppress artifacts caused by the effective boxcar windowing of the ideal interferogram originating from the finite path length range of the moving mirror. [1]

Since the resulting spectrum is the convolution of the frequency spectrum of the window function and the ideal spectrum, it is advantageous to apply a custom window function that has a narrow frequency spectrum and small side lobes. This process is called apodization and is widely used in FTIR spectroscopy. [1] One of the concerns in nano-FTIR (or DFTS) is how and what type of apodization to apply before the Fourier transform. Our main goal is to preserve the shape of the interferogram as much as possible because it contains the phase information of the sample.

4.1. Position of the ZPD and apodization

To collect as much useful information as possible, earlier works suggested setting the interferometer scanner range such that more of the positive OPD side of the interferogram is collected. [42] Thus, the ZPD position is shifted toward the beginning of the scanner range. However, it was not studied, if there is an optimal ZPD shift (interferogram position). In the following, we discuss this through measurements and simulations.

Connected to the ZPD shift, the question of the proper apodization naturally emerges. We cannot use a symmetric but shifted apodization function since it would become a combination of a boxcar function and the apodization function when the interferogram is shifted from the center. The application of an asymmetric apodization function was suggested previously by Amenabar et al., where the authors used an asymmetric three-term Blackman-Harris window. [42] This type of apodization, however, changes the symmetry of the interferogram when applied incorrectly and its effects were not discussed in detail before.

The effect of symmetry change can be dramatic on the phase spectrum. Let us suppose that the interferogram is symmetric at the beginning, i.e., there is no phase shift for any of the wavelength components in the broadband radiation. By shifting the ZPD position towards the beginning of the scanning range (shifting to the "left") and applying asymmetric apodization, we start to decrease the $\delta < 0$ side of the interferogram but keep the $\delta > 0$ side mostly untouched. In the extreme case, the ZPD location is at the very beginning of the scanner range and we only

[1] Storage rings can produce temporally coherent synchrotron radiation (CSR) resulting in very high-intensity THz pulses. Such sources are not considered here as CSR emission was only utilized for far-field spectroscopy measurements to date. [41]

measure the positive retardation side ($\delta > 0$) leading to a single-sided interferogram. This is equivalent to multiplying a double-sided interferogram with a Heaviside step function. The vanishing interferogram at retardations smaller than zero results in Kramers-Kronig relations in the complex spectrum. In other words, the Kramers-Kronig pair phase spectrum of the amplitude spectrum appears after the Fourier transform. [43,44] We demonstrate this effect in supplementary Section 2. and Fig. S2 on an originally symmetric interferogram. The additional phase introduced by the symmetry change can cause severe artifacts in the final spectrum that should be avoided. In the following, we systematically study the combined effect of ZPD position change and apodization on the final spectrum.

First, we measured the nano-FTIR interferogram of SiO_2/Si samples, just like in Section 3. In NeaSCOPE instruments, the scanning mirror is attached to a manual translation stage, which we can use to shift the whole assembly with a micrometer screw. This way we can change the location of the ZPD position within the range of the piezo scanner. In all our figures zero represents the middle of the scanner range, which would correspond to the location of the ZPD in a typical FTIR measurement with symmetric IFG. A series of measurements with different ZPD positions along the scanner range are shown in Fig. 6 (a) upper panel (raw). In the post-processing, we applied an asymmetric four-term Blackman-Harris window. Fig. 6 (a) lower panel (apodized) shows the apodization functions and the apodized interferograms. We used the same apodization for the reference interferograms measured with the same ZPD positions on gold and calculated the spectra using Eq. 10. The resulting spectra are shown in Fig. 6 (b).

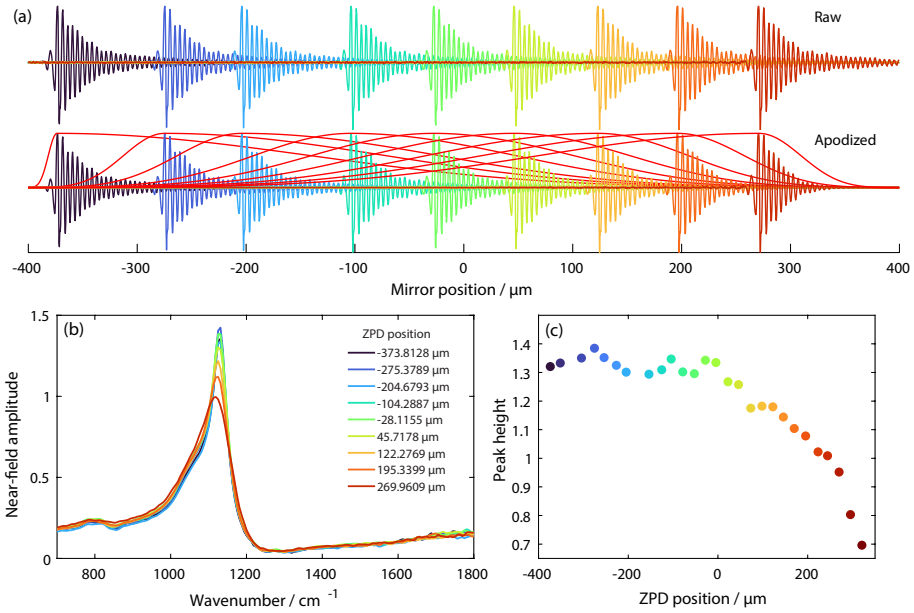

Fig. 6. (a) Measured SiO_2 near-field interferograms with different ZPD positions. (b) SiO_2 near-field spectra, calculated from the corresponding interferograms shown in (a) with different ZPD positions. (c) Magnitude of the SiO_2 phonon peak in each near-field spectra in (b).

As the interferogram is shifted to the positive side of the scanning range, the main phonon peak of silica broadens and decreases. This apparent reduction in spectral resolution is caused by the reduced interferogram length and the steeper apodization at positive values. This suggests that one should place the interferogram to the negative side of the scanning range to maximize spectral resolution for a fixed mirror scan length (and time). However, as we can see, there

is an optimum ZPD position (see in Fig. 6 (c)). If the interferogram is moved too far to the negative side, an insufficient portion of the interferogram is sampled and the rising part of the apodization function becomes so steep that even the short negative OPD side of the IFG gets distorted, resulting in a decrease in spectral peak height.

To further study the effect of the ZPD shift and the asymmetric apodization, we choose to simulate a more complex spectrum with different spectral features. We synthesized the interferograms with the help of Eq. 8 and calculated the spectra as described in Section 3. As a theoretical sample, we choose 30 nm of C_{60} fullerene molecules on top of the SiO_2/Si substrate. The spectrum then consists of the main phonon peak of the oxide and the four distinct narrow vibrational resonances of the high symmetry C_{60} molecules (526.53, 576.08, 1183.58, 1429.73 cm^{-1}). With such a complex spectrum, we can study the effects of the apodization on both the resolution and the relative spectral weights. The near-field amplitude and phase spectrum calculated by the FDM model are shown in Fig. S1. Below, Fig. 7 represents some of the interferograms and their corresponding apodization functions.

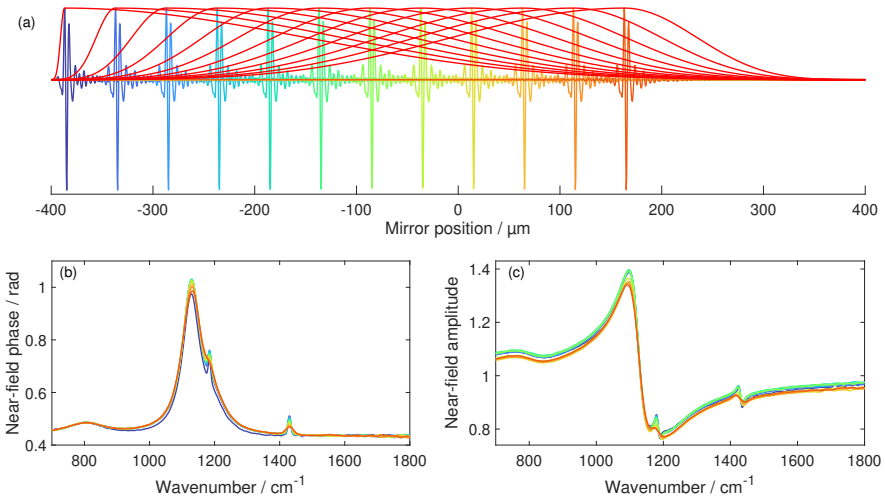

Fig. 7. (a) Calculated interferograms of the SiO_2/C_{60} layers for different ZPD positions with the corresponding asymmetric apodization function applied to them. (b) Phase and (c) amplitude spectra of the SiO_2/C_{60} system calculated from the interferograms corresponding to the color code.

In Fig. 7, we show the phase (b) and amplitude (c) spectra calculated from the interferograms displayed in (a). The main features in the spectrum are the SiO_2 phonon peak and two other peaks that correspond to the $T_{1u}(3)$ and $T_{1u}(4)$ vibrational modes of the C_{60} molecules in this spectral region. [45] The spectra clearly show that the resolution and the magnitude of the peaks decrease with increasing positive ZPD shifts, as discussed previously. For negative ZPD shifts the peak width monotonically decreases (resolution increases), however, after passing the ZPD position of $\approx -350\,\mu$m point, the 1183 cm^{-1} peak magnitude starts to decrease. Fig. 8 (a) and (b) we present the magnitude and the width of the peak at 1183 cm^{-1}, and (c) and (d) show the same values for the peak at 1429 cm^{-1}. We could see that the 1183 cm^{-1} C_{60} and the SiO_2 peak start to decrease after an optimum point but the peak 1429 cm^{-1} does not show the same behavior.

Besides our results give an insight of some trends about the effect of apodization they do not provide a clear answer if there is a specific optimum point of the ZPD position and thus the shape of the proper apodization function. Assessing only a few points of the spectrum does not describe the whole effect. The relative intensities of the peaks and the baseline of the spectra also change.

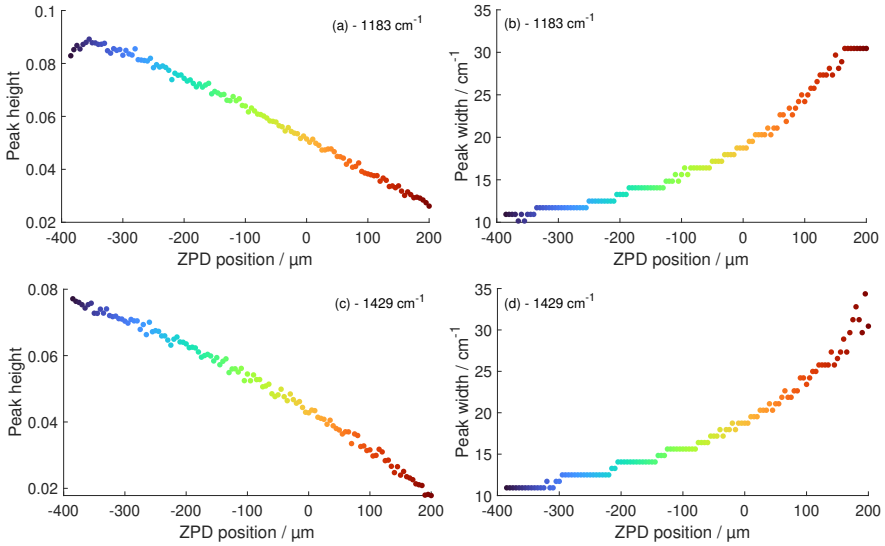

Fig. 8. (a) magnitude of the 1183 cm^{-1} C_{60} vibration, (b) width of the 1183 cm^{-1} peak, (c) magnitude of the 1429 cm^{-1} peak, (d) width of the 1429 cm^{-1} peak.

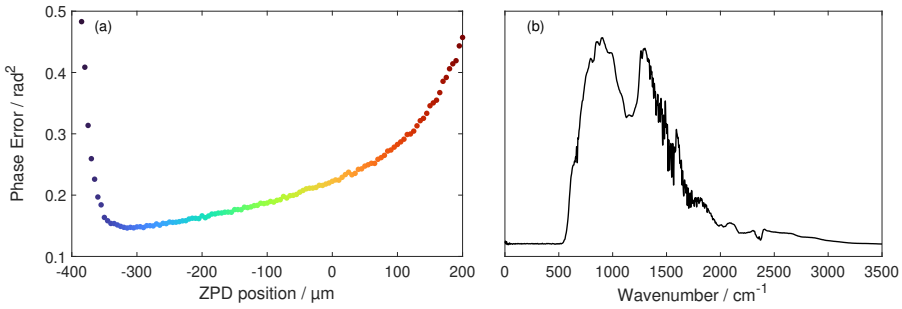

Fig. 9. (a) Error of the retrieved phase spectra compared to the ideal one for SiO_2/C_{60} system, calculated from interferograms with different ZPD positions (b) Light source spectrum used in the interferogram calculations.

For this, we define a measurement of phase error where we compare the spectrum calculated from the interferograms to the ideal spectrum calculated by the FDM model. This phase error is written as $\Delta S = \int_{\nu_1}^{\nu_2} (S_{IFG}(\nu) - S_{FDM}(\nu))^2 d\nu$, where ν_1 and ν_2 are the starting and ending wavenumber of the spectral region that we are interested in. We present this measure for all the simulated interferogram-spectra calculations with different ZPD shifts in Fig. 9. The figure shows that the phase error curve has a minimum at $ZPD_{\text{shift}} \approx -335\,\mu$m. The optimum ZPD shift corresponds to the minimum of the error curve. In other words, it is the optimum distance of the interferogram to the edge of the scanning range of the mirror.

The results shown above were calculated considering the broad infrared spectrum ($I_0(k)$, Fig. 9 (b)) of the SMIS beamline at Synchrotron SOLEIL, which was obtained by measuring the total signal before demodulation from a gold sample in the s-SNOM microscope. This measurement combines the effects of the source, optics, and detector to estimate the spectral response of the system. The ultrabroad wavelength range from synchrotron IR results in a

very narrow interferogram, as seen in the previous figures. Lab-based nano-FTIR systems, however, are typically equipped with infrared lasers based on difference frequency generation to produce an infrared output spectrum that has a much narrower spectrum than synchrotron radiation [33, 35]. This results in a much wider interferogram, which imposes an increased sensitivity to the apodization.

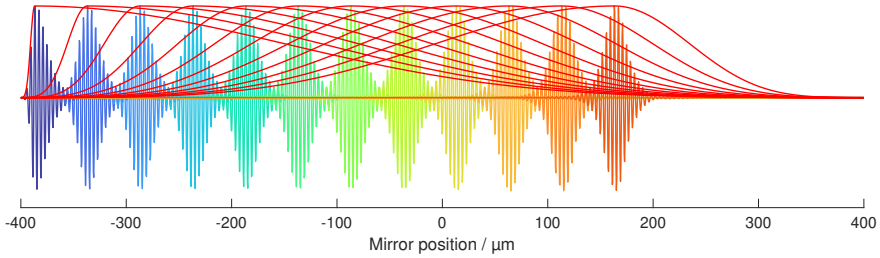

Fig. 10. Calculated interferograms of the SiO_2/C_{60} layers for different ZPD positions with the corresponding asymmetric apodization function applied. The light source spectrum is shown in Fig. 11 (b) resulting in the spatially spread interferograms.

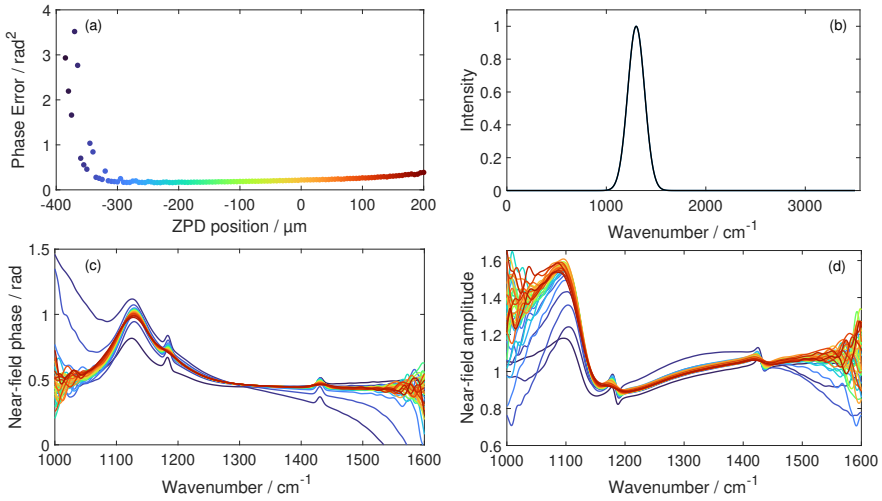

Fig. 11. (a) Phase error (ΔS) of the retrieved spectra compared to the ideal one for SiO_2/C_{60} system, calculated from interferograms with different ZPD positions. (b) Light source spectrum used to calculate the interferograms in Fig. 10. (c) phase and (d) amplitude spectra calculated from the corresponding interferograms. The dramatic effect of changing interferogram asymmetry is obvious in both amplitude and phase spectra.

We recalculated the interferograms for the same sample as before with a Gaussian spectrum centered at $1300\,\mathrm{cm}^{-1}$ with an FWHM = $200\,\mathrm{cm}^{-1}$. The corresponding interferograms are shown in Fig. 10. The figure shows that the spatially spread interferograms get distorted at smaller ZPD shifts than that of the broadband spectrum interferograms. Likewise, the spectral error of each shifted position, shown in Fig. 11 (a) reveals that a strong deviation of the resulting spectrum from the ideal occurs when the ZPD position is not chosen correctly.

We studied the effect of the interferogram width on the ideal position of the interferogram

and calculated the ideal ZPD position based on the minimum of the phase error for several light source spectra with different spectral widths. For all calculations, the phase error (ΔS) was calculated for the same spectral region between $\nu_1 = 900$ cm^{-1} and $\nu_2 = 1700$ cm^{-1}. The results presented in Fig. 12 clearly show that with decreasing spectral width, the optimum ZPD position is further and further away from the beginning of the scanner range.

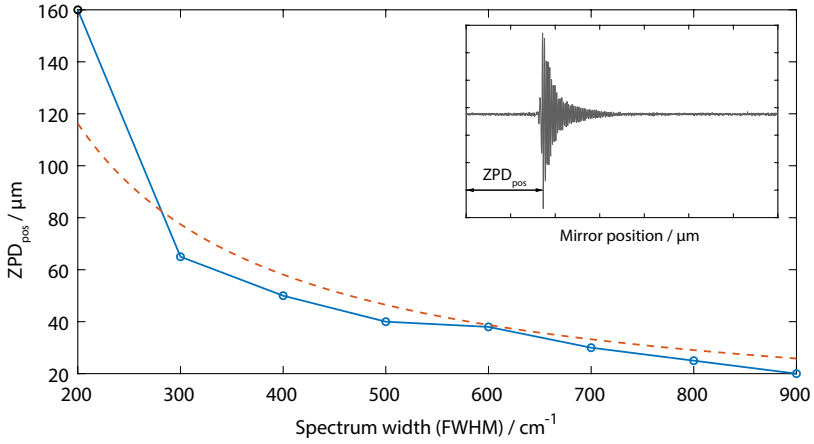

Fig. 12. Ideal ZPD position for different input spectrum widths (blue circles). The red dashed curve shows Eq. 12. The ZPD position is measured from the beginning of the scanner range as depicted in the inset.

We also aim to formulate how to find the ideal ZPD position depending on the spectral width of the light source. For the sake of simplicity, let us consider a light source with a Gaussian spectrum. From the FWHM of the light source spectrum (Δ_{LS}), we can calculate the width of the envelope of the interferogram (Δ_{IFG}), because the Fourier transform of a Gaussian is going to be also a Gaussian, thus:

$$\Delta_{IFG} = \frac{2}{\pi} \ln 2 / \Delta_{LS} \approx 0.44 / \Delta_{LS}. \tag{11}$$

As discussed, we want to keep the original shape of the interferogram as much as possible, thus the ZPD position has to be chosen accordingly. The ZPD position explicitly determines the steepness of the apodization function on both sides. To preserve the interferogram's shape we define a requirement that the 95% value point of the Blackmann-Harris apodization function has to coincide with the 50% point of the interferogram envelope (depicted in Fig. S5). This requirement results in

$$ZPD_{pos} \approx 2.3 / \Delta_{LS}. \tag{12}$$

In Eq. 12, ZPD_{pos} is measured from the beginning of the scanning range to easily implement during the scanner alignment. The result is plotted in Fig. 12 as the red dashed curve. Implementing this metric ensures that the spectrum is close to ideal and spectral phase component artifacts are minimized. Despite the good agreement between the derived formula and the numerical results, we want to note that it was derived for perfectly Gaussian light spectra resulting in a Gaussian interferogram envelope. In a more complex light spectrum, the interferogram can extend further to negative ZPDs thus being more vulnerable to the apodization. However, Eq. 12 can give a good approximation for the ZPD positioning, and the interferogram formulas in Eq. 8 help for more detailed analyses if needed. More details on the derivation of the optimal ZPD position equation can be found in the Supplementary Information material.

5. Conclusion

We showed that experimental nano-FTIR interferograms can be reproduced and understood in the framework of dispersive Fourier transform spectroscopy by choosing the proper insertion loss function defined by s-SNOM scattering models. Through simulations, we explained the ambiguity of coherent and non-coherent interferogram formation. We assessed the effect of apodization on the final spectrum and found that the preservation of interferogram asymmetry is key to obtaining an artifact-free phase spectrum. Based on our simulations, we provided a formula, for the first time, to determine an ideal shift for the ZPD position relative to the scanning range of the interferometer as a function of light source parameters.

6. Funding

This research used resources of Synchrotron SOLEIL and the Advanced Light Source (a DOE Office of Science User Facility under contract no. DE-AC02-05CH11231).

7. Acknowledgement

The authors thank Prof. T. J. Parker for offering his insights on the DFTS technique.

8. Disclosure

The authors declare no conflicts of interest.

References

1. P. R. Griffiths, "The early days of commercial FT-IR spectrometry: A personal perspective," Appl. Spectrosc. **71**, 329–340 (2017).
2. P. Fellgett, "The theory of infra-red sensitivities and its application to investigations of stellar radiation in the near infra-red," Ph.D. thesis, University of Cambridge (1951).
3. P. Jacquinot, "The luminosity of spectrometers with prisms, gratings, or Fabry-Perot etalons," J. Opt. Soc. Am. **44**, 761–765 (1954).
4. A. A. Michelson and E. W. Morley, "On the relative motion of the earth and the luminiferous ether," Am. J. Sci. **s3-34**, 333–345 (1887).
5. R. de L. Kronig, "On the theory of dispersion of x-rays," J. Opt. Soc. Am. **12**, 547 (1926).
6. H. A. Kramers, "La diffusion de la lumiere par les atomes," Atti Congr. Intern. Fisici (Transactions Volta Centen. Congr. Como **2**, 545–557 (1927).
7. J. E. Chamberlain, J. E. Gibbs, and H. A. Gebbie, "Refractometry in the far infra-red using a two-beam interferometer," Nature **198**, 874–875 (1963).
8. E. E. Bell, "The use of asymmetric interferograms in transmittance measurements," Le J. de Physique Colloques **28**, C2–18–C2–25 (1967).
9. J. R. Birch, "Dispersive fourier transform spectroscopy," Microchim. Acta **93**, 105–122 (1987).
10. T. J. Parker, "Dispersive fourier transform spectroscopy," Contemp. Phys. **31**, 335–353 (1990).
11. J. R. Birch and T. J. Parker, *Infrared and Millimeter Waves, Volume 2, Instrumentation* (Academic Press, 1979), chap. Dispersive Fourier Transform Spectrometry.
12. T. J. Parker, Personal Communication.
13. N. Ocelic, A. Huber, and R. Hillenbrand, "Pseudoheterodyne detection for background-free near-field spectroscopy," Appl. Phys. Lett. **89**, 101124 (2006).
14. F. Huth, M. Schnell, J. Wittborn, N. Ocelic, and R. Hillenbrand, "Infrared-spectroscopic nanoimaging with a thermal source," Nat. Mater. **10**, 352–356 (2011).
15. X. Chen, Z. Yao, S. G. Stanciu, D. N. Basov, R. Hillenbrand, and M. Liu, "Rapid simulations of hyperspectral near-field images of three-dimensional heterogeneous surfaces," Opt. Express **29**, 39648–39668 (2021).
16. X. Chen, Z. Yao, Z. Sun, S. G. Stanciu, D. N. Basov, R. Hillenbrand, and M. Liu, "Rapid simulations of hyperspectral near-field images of three-dimensional heterogeneous surfaces - part II," Opt. Express **30**, 11228–11242 (2022).
17. P. McArdle, D. J. Lahneman, A. Biswas, F. Keilmann, and M. M. Qazilbash, "Near-field infrared nanospectroscopy of surface phonon-polariton resonances," Phys. Rev. Res. **2**, 023272 (2020).
18. A. S. McLeod, P. Kelly, M. D. Goldflam, Z. Gainsforth, A. J. Westphal, G. Dominguez, M. H. Thiemens, M. M. Fogler, and D. N. Basov, "Model for quantitative tip-enhanced spectroscopy and the extraction of nanoscale-resolved optical constants," Phys. Rev. B **90**, 085136 (2014).
19. B.-Y. Jiang, L. M. Zhang, A. H. Castro Neto, D. N. Basov, and M. M. Fogler, "Generalized spectral method for near-field optical microscopy," J. Appl. Phys. **119**, 054305 (2016).

20. S. T. Chui, X. Chen, M. Liu, Z. Lin, and J. Zi, "Scattering of electromagnetic waves from a cone with conformal mapping: Application to scanning near-field optical microscope," Phys. Rev. B **97**, 081406 (2018).
21. A. Cvitkovic, N. Ocelic, and R. Hillenbrand, "Analytical model for quantitative prediction of material contrasts in scattering-type near-field optical microscopy," Opt. Express **15**, 8550–8565 (2007).
22. B. Hauer, A. P. Engelhardt, and T. Taubner, "Quasi-analytical model for scattering infrared near-field microscopy on layered systems," Opt. Express **20**, 13173–13188 (2012).
23. D. Datz, G. Németh, L. Rátkai, A. Pekker, and K. Kamarás, "Generalized mie theory for full-wave numerical calculations of scattering near-field optical microscopy with arbitrary geometries," physica status solidi (RRL) – Rapid Res. Lett. **n/a**, 2300370 (2023).
24. G. Németh, K. Otsuka, D. Datz, A. Pekker, S. Maruyama, F. Borondics, and K. Kamarás, "Direct visualization of ultrastrong coupling between luttinger-liquid plasmons and phonon polaritons," Nano Lett. **22**, 3495–3502 (2022). PMID: 35315666.
25. Z. Fei, A. S. Rodin, G. O. Andreev, W. Bao, A. S. McLeod, M. Wagner, L. M. Zhang, Z. Zhao, M. Thiemens, G. Dominguez, M. M. Fogler, A. H. C. Neto, C. N. Lau, F. Keilmann, and D. N. Basov, "Gate-tuning of graphene plasmons revealed by infrared nano-imaging," Nature **487**, 82–85 (2012).
26. Z. Fei, G. O. Andreev, W. Bao, L. M. Zhang, A. S McLeod, C. Wang, M. K. Stewart, Z. Zhao, G. Dominguez, M. Thiemens, M. M. Fogler, M. J. Tauber, A. H. Castro-Neto, C. N. Lau, F. Keilmann, and D. N. Basov, "Infrared nanoscopy of Dirac plasmons at the graphene-sio2 interface," Nano Lett. **11**, 4701–4705 (2011).
27. F. H. L. Koppens, D. E. Chang, and F. J. García de Abajo, "Graphene plasmonics: A platform for strong light–matter interactions," Nano Lett. **11**, 3370–3377 (2011).
28. A. M. Gigler, A. J. Huber, M. Bauer, A. Ziegler, R. Hillenbrand, and R. W. Stark, "Nanoscale residual stress-field mapping around nanoindents in sic by ir s-snom and confocal raman microscopy," Opt. Express **17**, 22351–22357 (2009).
29. S. Dai, Q. Ma, Y. Yang, J. Rosenfeld, M. D. Goldflam, A. McLeod, Z. Sun, T. I. Andersen, Z. Fei, M. Liu, Y. Shao, K. Watanabe, T. Taniguchi, M. Thiemens, F. Keilmann, P. Jarillo-Herrero, M. M. Fogler, and D. N. Basov, "Efficiency of launching highly confined polaritons by infrared light incident on a hyperbolic material," Nano Lett. **17**, 5285–5290 (2017). PMID: 28805397.
30. L. M. Zhang, G. O. Andreev, Z. Fei, A. S. McLeod, G. Dominguez, M. Thiemens, A. H. Castro-Neto, D. N. Basov, and M. M. Fogler, "Near-field spectroscopy of silicon dioxide thin films," Phys. Rev. B **85**, 075419 (2012).
31. W. Ma, P. Alonso-González, S. Li, A. Y. Nikitin, J. Yuan, J. Martín-Sánchez, J. Taboada-Gutiérrez, I. Amenabar, P. Li, S. Vélez, C. Tollan, Z. Dai, Y. Zhang, S. Sriram, K. Kalantar-Zadeh, S.-T. Lee, R. Hillenbrand, and Q. Bao, "In-plane anisotropic and ultra-low-loss polaritons in a natural van der waals crystal," Nature **562**, 557–562 (2018).
32. J. Kischkat, S. Peters, B. Gruska, M. Semtsiv, M. Chashnikova, M. Klinkmüller, O. Fedosenko, S. Machulik, A. Aleksandrova, G. Monastyrskyi, Y. Flores, and W. T. Masselink, "Mid-infrared optical properties of thin films of aluminum oxide, titanium dioxide, silicon dioxide, aluminum nitride, and silicon nitride," Appl. Opt. **51**, 6789–6798 (2012).
33. F. Huth, A. Govyadinov, S. Amarie, W. Nuansing, F. Keilmann, and R. Hillenbrand, "Nano-ftir absorption spectroscopy of molecular fingerprints at 20 nm spatial resolution," Nano Lett. **12**, 3973–3978 (2012). PMID: 22703339.
34. S. Amarie, P. Zaslansky, Y. Kajihara, E. Griesshaber, W. W. Schmahl, and F. Keilmann, "Nano-ftir chemical mapping of minerals in biological materials," Beilstein J. Nanotechnol. **3**, 312–323 (2012).
35. F. Keilmann and S. Amarie, "Mid-infrared frequency comb spanning an octave based on an er fiber laser and difference-frequency generation," J. Infrared, Millimeter, Terahertz Waves **33**, 479–484 (2012).
36. D. J. Lahneman, T. J. Huffman, P. Xu, S. L. Wang, T. Grogan, and M. M. Qazilbash, "Broadband near-field infrared spectroscopy with a high temperature plasma light source," Opt. Express **25**, 20421–20430 (2017).
37. H. A. Bechtel, E. A. Muller, R. L. Olmon, M. C. Martin, and M. B. Raschke, "Ultrabroadband infrared nanospectroscopic imaging," Proc. National Acad. Sci. **111**, 7191–7196 (2014).
38. S. Amarie, T. Ganz, and F. Keilmann, "Mid-infrared near-field spectroscopy," Opt. Express **17**, 21794–21801 (2009).
39. F. A. Hopf, R. F. Shea, and M. O. Scully, "Theory of optical Free-Induction decay and Two-Photon superradiance," Phys. Rev. A **7**, 2105–2110 (1973).
40. G. Duxbury, J. F. Kelly, T. A. Blake, and N. Langford, "Observation of infrared free-induction decay and optical nutation signals from nitrous oxide using a current modulated quantum cascade laser," J. Chem. Phys. **136**, 174317 (2012).
41. Åke Andersson and Matthew S Johnson and Bengt Nelander, "Coherent synchrotron radiation in the far infrared from a 1-mm electron bunch," Opt. Eng. **39**, 3099–3105 (2000).
42. I. Amenabar, "Infrared nanospectroscopy and hyperspectral nanoimaging of organic matter," Ph.D. thesis, University of the Basque Country (2017).
43. "A simple derivation of the kramers-kronig relations from the perspective of system theory," https://www.iam.kit.edu/et/plainhtml/Download/Derivation_Kramers-Kronig.pdf. Accessed: 2023-09-27.
44. D. K. M. Schönleber and E. Ivers-Tiffée, "A method for improving the robustness of linear kramers-kronig validity tests," Electrochimica Acta pp. 20–27 (2014).
45. W. Krätschmer, K. Fostiropoulos, and D. R. Huffman, "The infrared and ultraviolet absorption spectra of laboratory-produced carbon dust: evidence for the presence of the C_{60} molecule," Chem. Phys. Lett. **170**, 167–170 (1990).